

Improved Electrochemical Performances of Ti-Fe Based Alloys by Mechanical Milling

Zhong-gang Han¹, Ting-ting Zhai¹, Ze-ming Yuan^{1,3,*}, Fu-chen Liu¹,
Dian-chen Feng^{1,3}, Hao Sun¹, Yang-huan Zhang^{2,*}

¹ School of Materials and Metallurgy, Inner Mongolia University of Science and Technology, Baotou 014010, China

² Department of Functional Material Research, Central Iron and Steel Research Institute, Beijing 100081, China

³ Collaborative Innovation Center of Integrated Exploitation of Bayan Obo Multi-Metal Resources, Inner Mongolia University of Science and Technology, Baotou 014010, China)

*E-mail: zmyuan153@163.com (ZM Yuan), zhangyh59@sina.com (Y.H. Zhang)

Received: 25 October 2022 / Accepted: 1 December 2022 / Published: 27 December 2022

In this paper, ball milling alloy powder was prepared by mechanical ball milling of $\text{Ti}_{1.04}\text{Zr}_{0.1}\text{La}_{0.06}\text{Fe}_{0.6}\text{Ni}_{0.3}\text{Mn}_{0.2}$ hydrogen storage alloy synthesized in a vacuum induction melting furnace in a planetary ball mill. After that, electrode sheets for electrochemical testing were produced by a tablet press, and the effects of ball milling time on the phase structure, microscopic morphology, and electrochemical properties of the alloy were investigated. The results show that the primary alloy is composed of the main phase TiFe phase, secondary phase ZrMn_2 and a small amount of La phase. The diffraction peaks occurred significantly broadened and the ZrMn_2 phase gradually disappeared with the extension of the ball milling time. By observing the surface morphology of the alloy using SEM, and it was found that the size of the alloy particles became significantly smaller in short-time ball milling, while long-interval ball milling resulted in agglomeration of the alloy particles. Meanwhile, the electrochemical performance test showed that mechanical ball milling could significantly improve the activation performance and electrochemical capacity of the alloy, and the alloy achieved the maximum first discharge capacity of 252.5 mAh/g after 1h of ball milling, as well as the highest cyclic stability among the 30h specimens. The high rate discharge performance (HRD) first increased and then decreased with the increase of ball milling time, and the maximum HRD value of 54.63% was obtained at a current density of 80 mA/g for the 1h ball milling alloy. The trends of the kinetic parameters (hydrogen diffusion coefficient (D), ultimate current density (I_L), and AC impedance (R_{ct})) all reflect the pattern of the high-rate discharge performance (HRD). The research indicates that short-time high-energy ball milling (HEBM) can improve the electrochemical properties of TiFe hydrogen storage alloy.

Keywords: TiFe hydrogen storage alloy; Mechanical ball milling; Microstructure; Electrochemical properties

1. INTRODUCTION

As one of the highly promising and desirable clean energy sources, hydrogen energy has attracted the attention and pursuit of scholars in recent years, and the key to the current technology of hydrogen energy utilization is the development of safe and efficient, inexpensive storage media [1, 2]. With the rapid development of new energy vehicles in recent years and the emergence of a number of new Internet car-manufacturers forces, it has brought infinite vitality and opportunities to the domestic automobile industry market. As the primary power source of electric vehicles, a power battery is an essential key component to promote the development of new energy vehicles. Several global leading Chinese battery companies have also been created in rapid development background. Around the upstream and downstream of the industrial chain, there are also a lot of industrial opportunities, and the development of new energy power batteries will enter a new track.

Ni-MH power battery has just entered the maturity stage and is the only battery system used in hybrid vehicles that have been practically verified, commercialized, and scaled up. 99% of the existing hybrid batteries are Ni-MH batteries, and the representative of commercialization is Toyota's Prius. Its advancement has achieved high evaluation worldwide. To realize the practical industrial application of new energy power, researchers have done much research in the past four decades, including AB₅-type, AB₂-type, AB-type, A₂B-type, and V-based solid solution [3, 4]. Unfortunately, there is no mature material to meet the requirements of the U.S. Department of Energy for the automotive industry, but the high capacity, high endurance, and safety of Ni-MH batteries make them more compatible with the requirements of portable power and hybrid electric vehicle (HEV) power [5, 6]. Ni-MH batteries are designed and manufactured on the basis of the electrochemical properties of hydride compounds. Due to the low hydrogen absorption and discharge capacity of RE-based AB₅-type hydrogen storage material as anode material, Ni-MH batteries do not have an advantage over Li-batteries [7]. Therefore, it is urgent to develop new batteries with better performance.

TiFe-based intermetallic compounds are typical representatives of AB-type alloys. TiFe alloys have attracted extensive attention since they were discovered by Reilly and Wiswall in 1974 [8]. Researchers have found many excellent properties for fuel cells as an auspicious anode material. TiFe-based hydrogen storage alloys have moderate hydrogen release pressure, the operating temperature near room temperature, low cost, high hydrogen storage capacity (1.86 wt.%) at room temperature and a fast hydrogen kinetics [9, 10]. However, the main problem of TiFe-based alloys as hydrogen storage materials is the difficulty of activation. The alloy must be activated at 3-5 MPa hydrogen pressure and 673 K before it can absorb hydrogen, which limits the commercial application of this system alloy [11, 12]. To minimize the activation temperature of alloys and shorten the incubation period, a number of excellent methods have been discovered by researchers over the years, mainly including stoichiometric design, plastic deformation, surface modification, mechanical ball milling, and new manufacturing techniques.

The TiFe-based hydrogen storage alloy samples prepared by HEBM contain nano-scale TiFe intermetallic compounds and nano-scale TiFe solid solutions. Their discharge capacity is significantly higher than the as-cast alloys prepared by arc melting technology without ball milling. Therefore, mechanical ball mill is an efficient and powerful method to prepare and improve the electrochemical

properties of anode materials for new energy batteries. Consequently, researchers [13-17] have conducted much research in recent years, expecting to prepare TiFe-based alloys by mechanical alloying to improve their activation properties. In addition, the study also found that under the action of mechanical energy, each element in the alloy achieves alloying in the solid-state. The ball-milled alloy obtained by Shang et al. [18] significantly reduced the grain size of the alloy by mechanical ball-milling, and a large number of nanocrystalline and amorphous structures appeared in ball milling. Meanwhile, Abrashev et al. [19] concluded that the phase structure, crystal size and lattice defects within the alloy would be changed through mechanical alloying, promoting the formation of nanocrystalline and amorphous structures. Emami et al. [20] prepared TiFe alloys by mechanical ball milling and studied their activation properties. It was found that the as-cast alloys were all large particles before ball milling, and the grain size could be reduced to about 7 nm after ball milling. A refined alloy will have a large specific surface area after grinding the grains, provides more interfaces and channels for H molecules to enter the alloy interior, and significantly improves the kinetic properties. At the same time, it improved the activation capability of TiFe alloy and can absorb 1.5 wt.% of hydrogen directly at 303 K without any treatment. Zeaiter et al. [21] also studied the performance of hydrogen storage was also investigated after short-time ball milling. They reported that ball milling for short periods of time increases particle surface area and decreases particle diameter. Due to this modification of the microstructure, the activation performance is improved. Meanwhile, the hydrogen absorption and desorption plateau pressure were reduced. TiFe alloys can also benefit from elemental alloying by enhancing their activation and hydrogen storage capabilities [22, 23]. The replacement of Ti by rare earth elements (La, Ce, Pr, Nd, Y, Sm) [24-29] or partial replacement of Fe or Ti in TiFe series alloys using the transition group elements Mn, Ni, Cr, Co, Zr, Al, V, Pd, etc. [30-35] has significantly improved the activation performance of the alloys as well as the hydrogen absorption kinetics and thermodynamic properties. Ball milling is a powerful and effective way to prepare and improve the electrochemical properties of anode materials for new energy batteries [20]. Since TiFe has an electrochemical theoretical capacity over 400 mAh/g, it can also serve as a potential electrode material. Unfortunately, electrochemical studies of materials are often overlooked. Today, the main obstacles to achieving the commercial application of TiFe-based alloys are their low discharge performance, slow kinetics, and harsh activation conditions. Surface oxides and passivation layers are the main culprits for the problems listed above [15]. Jain et al. [36] demonstrated that adding an appropriate amount of Zr to TiFe alloy resulted in the formation of a Zr-rich second phase, which would make the alloy easier to form an intergranular content or Zr-rich phase, promoting the entry of H atoms and significantly improve the activation performance of the experimental alloy, and the experimental alloy can directly absorb hydrogen without the incubation time. Moreover, by substituting Fe for V, Mn and Pd, the reversible capacity can be increased, $\text{TiFe}_{0.8}\text{Pd}_{0.1}\text{V}_{0.1}$ and $\text{TiFe}_{0.9}\text{Pd}_{0.1}$ have capacities exceeding 400 mAh/g and 200 mAh/g, respectively, when Fe is replaced with V, Mn, and Pd [37, 38]. Seiler et al. [39] found that Mn could segregate on the surface of TiFe alloy by forming an oxide layer, thereby promoting the diffusion of H atoms. As a result of Mn addition, alloy defect density and surface oxide layer increase, which improves the H atoms diffusion path, and activation properties. Because Mn enhances hydrogen dis/absorption without reducing the hydrogen storage capacity of the alloy, and it was considered the optimal elemental substitution choice [40]. Patel et al. [10] reported that when Zr and Mn are added together to TiFe alloys to obtain mutual synergy, better kinetic properties and

capacity can be obtained compared to adding Zr or Mn elements alone. The element Ni partially replacing Fe can also form NiO, which adheres to the particles surface with TiO₂ and FeO, reducing the compactness of the surface and promoting the diffusion of hydrogen atoms, thus improving the activation properties [41]. In addition, the flattening trend of the hydrogen release plateau while forming solid solution in TiFe-based alloys is not adversely affected by adding element Ni, and the transition group element Ni also promotes the kinetic properties of alloy [42].

Activation properties of TiFe alloys can also be improved by adding rare earth elements. Rare earth elements do not dissolve into the matrix phase but are distributed in the form of tiny particles or agglomerates in the interstitial positions. Because rare earth elements can easily absorb hydrogen to form hydrides, they become activation sites in the hydrogen absorption process and produce the "hydrogen pumping effect" [43], so they can accelerate the activation process. Leng et al. [44] investigated that at 353 K and 4 MPa, TiFe_{0.9}Mn_{0.1} alloy could absorb hydrogen directly when small quantities of Ce and Mn were added, while the TiFe_{0.9}Mn_{0.1} alloy without the addition of Ce required a gestation period of 2 h under the same conditions. It was found that the formation of hydrides of Ce during the hydrogen absorption process was facilitated.

Based on the previous work, the Ti_{1.04}Zr_{0.1}La_{0.06}Fe_{0.6}Ni_{0.3}Mn_{0.2} alloy prepared in the vacuum induction melting furnace was used as the experimental material, and then the as-cast alloy was ball-milled for 0, 1, 5, 20, and 30 h. The effect of ball milling time on the microscopic morphology, phase structure, and electrochemical properties of TiFe alloys was analyzed. A new type of battery anode material with excellent electrochemical properties was expected to be obtained through element substitution and mechanical ball milling.

2. EXPERIMENTAL

The alloy was prepared according to the composition of Ti_{1.04}Zr_{0.1}La_{0.06}Fe_{0.6}Ni_{0.3}Mn_{0.2}, and it was produced in a vacuum induction melting furnace by melting Ti sponge, Zr sponge, pure iron, Ni plate, electrolytic Mn and RE elements in the form of cast ingots (purity of raw metal $\geq 99.9\%$). Mn and rare earth elements were added more than 5% by mass to account for losses due to volatilization, as they have lower melting and boiling points than Ti, Fe, Ni, and Zr elements. The melting process was carried out under 0.04 MPa helium protection, and the obtained liquid metal was poured into a metal mold and cooled to room temperature. The ingots were then mechanically crushed and then ground into powder using a grinder and passed through a 200-mesh standard sieve to obtain a 200-mesh cast powder alloy, which was then ball-milled (model number: QM-3SP2; manufacturer: Nanjing Chi Shun Technology Development Co., Ltd). The ball milling process is mainly divided into the following three steps: (a) Put 400 g of stainless steel balls into the ball mill can in the vacuum glove box, including 2 balls of 20 mm, 20 balls of 10 mm, and all other balls of 6 mm. Afterwards, 10 g of experimental alloy powder was added to the ball mill can, the ball to the material is 40:1. (b) The ball mill tank was sealed in a vacuum glove box environment. (c) Install the ball mill can on the ball mill, set the ball milling speed to 350 r/min, and set the ball milling time to 1, 5, 20, and 30 h, respectively. The ball mill was suspended every 1 h and the suspension time was 0.5 h, which could prevent the sample from overheating and loss during the ball

milling process. The ball-milled alloy powder was filtered through a 300-mesh sieve to obtain a ball-milled sample, which was sealed under vacuum before storage.

The 15 mm diameter electrode sheets were produced by mixing 0.2 g of powder with 0.8 g of carbonyl Ni and holding them under pressure at 25 MPa for 5 min. Then the pressed electrode sheets were wrapped with nickel foam, connected with the electrode sheets by nickel strip leads and fixed as lugs, fixed around with sharp-nosed pliers, and labeled with the name and quality, and the alloy electrode sheets required for the experiment.

The phase composition and structure of the experimental samples were collected using a D8-Advance X-ray diffractometer with a Cu source, the operating voltage of 40 kV, range $20^{\circ}\sim 90^{\circ}$ (2θ), and step size 0.02° . The sample morphology was observed by scanning electron microscope (SEM) (QUANTA 400). Energy dispersive spectroscopy was also used to observe the elemental composition of each phase of the as-cast bulk sample. The electrochemical properties of the experimental alloys were measured using a CT2001A cell test system manufactured by Wuhan Blue Battery and maintained in a water bath at 30°C . An open-ended three-electrode system was used with 6 mol/L KOH + 15 g/L LiOH solution as the electrolyte, sintered NaOH as the auxiliary electrode, and Hg/HgO as the reference electrode. The voltage between the negative electrode and the reference one was defined as the discharge voltage. In the alloy capacity test, the charge-discharge current density is 40 mA/g, the cut-off voltage is 0 V (vs. Hg/HgO), and a total of 20 cycles are used; in the cycle stability test, the charge-discharge current density is 200 mA/g, and the cut-off voltage is -0.5 V (vs. Hg/HgO), 20 cycles in total; High rate discharge performance is charged at 40 mA/g current density after activation, then discharged at 40, 80, 120, 160 and 200 mA/g current density respectively, and the cut-off voltage is -0.5 V (vs. Hg/HgO). After the sample was activated, an electrochemical impedance test (frequency 10000 Hz \sim 0.005 Hz, amplitude 5 mV) and potentiodynamic polarization test (scanning range: -0.5 V \sim 1.2 V) were carried out on the electrode sheet with a depth of discharge (DOD) of 50% by PARSTAT-4000 electrochemical workstation, perform a constant potential step test on the fully charged electrode (step potential 0.25 V, duration 3600 s).

3. RESULTS AND DISCUSSION

3.1. Microstructure characterization

Fig. 1 demonstrates the XRD pattern of $\text{Ti}_{1.04}\text{Zr}_{0.1}\text{La}_{0.06}\text{Fe}_{0.6}\text{Ni}_{0.3}\text{Mn}_{0.2}$ alloy milled with different time. According to the data of the International Diffraction Center, there is a sharp and narrow crystal diffraction peak in the cast alloy, and the as-cast alloys can be monitored with distinctive three strong peaks and the positions of the peaks are $2\theta=42.4^{\circ}$, 62.0° and 78.1° respectively. The as-cast alloy can be monitored to have three strong peaks, and the positions of the peaks are $2\theta=42.4^{\circ}$, 62.0° , and 78.1° , which are considered to be body-centered cubic TiFe main phase of structure (PDF#65-4398; Pm-3m (110)). In addition, the remaining diffraction peaks are most probably the phase of ZrMn_2 (PDF#39-1013; P63/mmc (194)), while the other small diffraction peaks are probably the rare earth La phase. All diffraction peaks of the ball-milled samples correspond strictly and without shifts, so despite ball milling,

the alloy's phase composition does not change. However, as the ball milling time gradually increased from 1 h to 30 h, the diffraction peaks broadened significantly, the diffraction

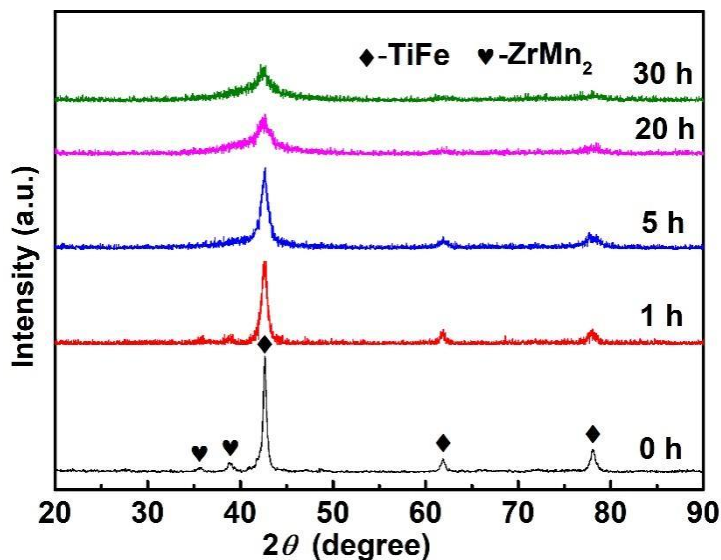


Figure 1. XRD profiles of the as-milled $Ti_{1.04}Zr_{0.1}La_{0.06}Fe_{0.6}Ni_{0.3}Mn_{0.2}$ alloy.

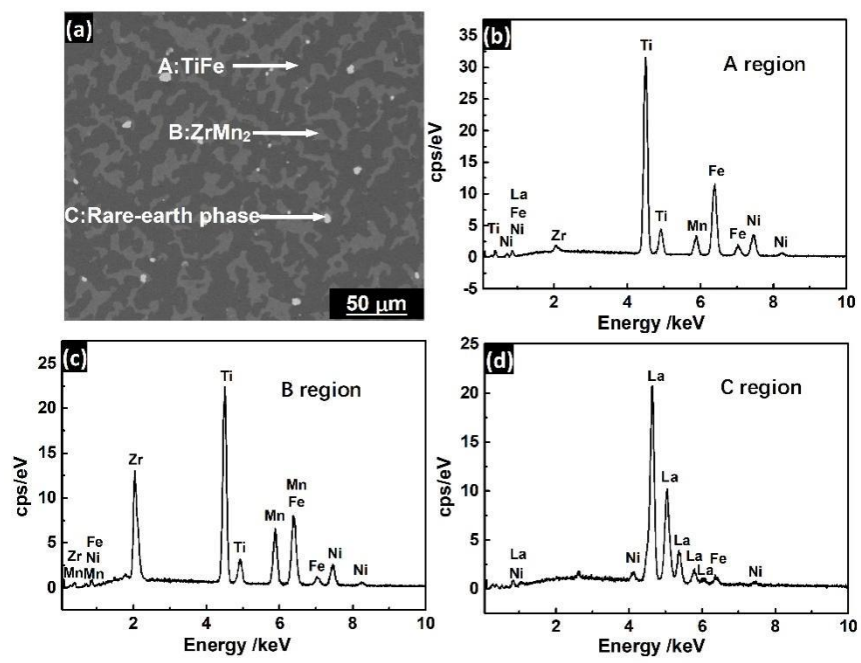


Figure 2. (a) SEM morphologies of $La_{0.06}$ alloy; (b) EDS patterns of the TiFe phase; (c) EDS patterns of the $ZrMn_2$ phase; (d) EDS patterns of the rare earth La phase.

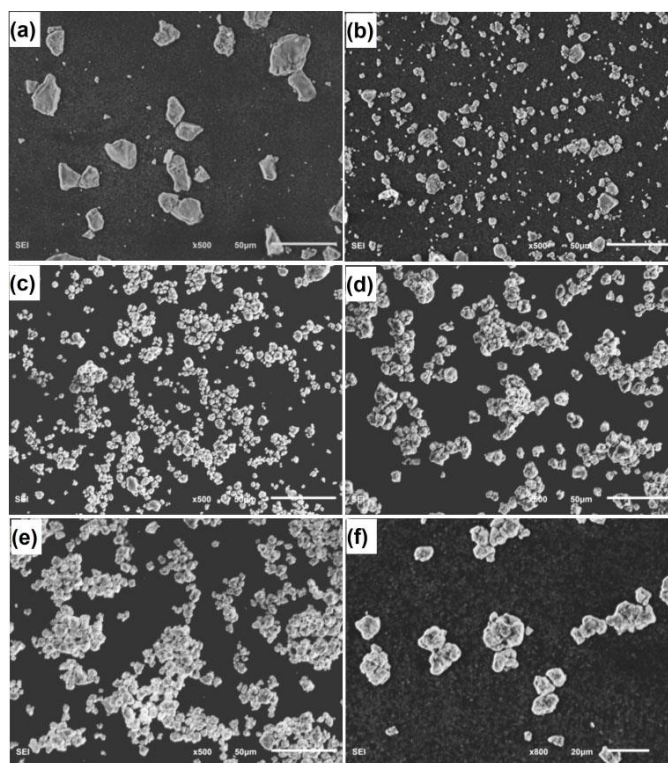


Figure 3. Morphology of the as-milled $\text{Ti}_{1.04}\text{Zr}_{0.1}\text{La}_{0.06}\text{Fe}_{0.6}\text{Ni}_{0.3}\text{Mn}_{0.2}$ alloy: (a) 0 h milling; (b) 1 h milling; (c) 5 h milling; (d) 20 h milling; (e) 30 h milling; (f) 30 h milling (800 \times).

intensity decreased, and some of the weaker peaks of the as-cast alloy were no longer observed after five hours of ball milling, and the ZrMn_2 and La phases disappeared. These changes indicate that the grain size of the alloy has been reduced, and the crystalline state gradually changes to finer nanocrystals or amorphous. As reported by Hosni et al. [31], titanium, iron and manganese elements are no longer displayed in the TiFe alloy milled for 40h, and the diffraction peak is obviously broadened and the alloy is amorphous.

In Fig. 2, the energy spectrum detection of various sections of the parent alloy is carried out. The detection area of the experimental samples is shown in Fig. 2 (a). From the energy spectrum analysis of Figs. 2 (b) ~ (d), it can be seen that the grey and black area is the main phase TiFe, the gray area is the second phase of ZrMn_2 segregated on the TiFe phase, and the white area is the rare earth La phase.

Particle size and surface state play an important role in improving hydrogen storage properties of hydrogen storage alloys. Therefore, it is necessary to observe alloy grains' appearance changes with ball milling time. From Fig. 3 (a), it can observe that the grain size of the unballasted alloy powder is more extensive, with sharp edges and corners, and the shape is irregular, according to Figs. 3 (b) and (c), mechanical ball milling will lead to noticeable size reduction. Moreover, the size of alloy particles is also decreasing with the lengthening of ball milling time. The alloy powder has good dispersion, but the particle size is not uniform. As the ball milling time extends to 5 h, the alloy particles begin to agglomerate. Ball milling for more than 20 hours will produce a more serious agglomeration phenomenon. This is due to the reduction of particle size by mechanical ball milling and the increase of surface energy due to the increase in surface defects. It can also see that after ball milling, the grains become smoother, the edges and corners gradually disappear, and the shape becomes more regular.

It should be noted that the alloy surface does not show significant cracking, unlike the former reports [45,46], since the particle radius is already so small that it is difficult to break down to smaller sizes. That agglomeration of particle grains leads to a decrease in the degree of particle refinement and an increase in specific surface area. Particle agglomeration is a normal phenomenon in mechanical ball milling. In a study by Zhang [47] et al, high-energy ball milling of $Mg_{20-x}Y_xNi_{10}$ ($x=0, 1, 2, 3,4$) alloys was performed and severe agglomeration was found to occur in ball milled alloys, and the same agglomeration occurred in ball milled $La_9Ce_1Mg_{80}Ni_5$ -Ni-GR alloy [48]. Ulate-Kolitsky et al. [49] also found that agglomeration of TiFe-Mn-Zr alloy started to occur after 10 min of ball milling. The ball milling process inhibits agglomeration for many reasons, but all are detrimental to the alloy's activation and electrochemical behavior.

3.2 Electrochemical performance

A hydrogen storage alloy's electrochemical properties primarily include activation, discharge, and voltage characteristics. An alloy with good activation capabilities is essential for hydrogen storage. Activation is maximizing the discharge capacity by multiple charging and discharging. In general, electrodes with fewer cycles have a higher activation capacity. In terms of discharge capacity, the base alloy has a very low capability. In a study by Jurczyk et al. [50], TiFe was reported to have a 0.7 mAh/g discharge capacity. Furthermore, the maximum discharge capacity of the nanocrystalline TiFe-type alloy synthesized by M. Jurczyk et al is 155 mAh/g.[51]

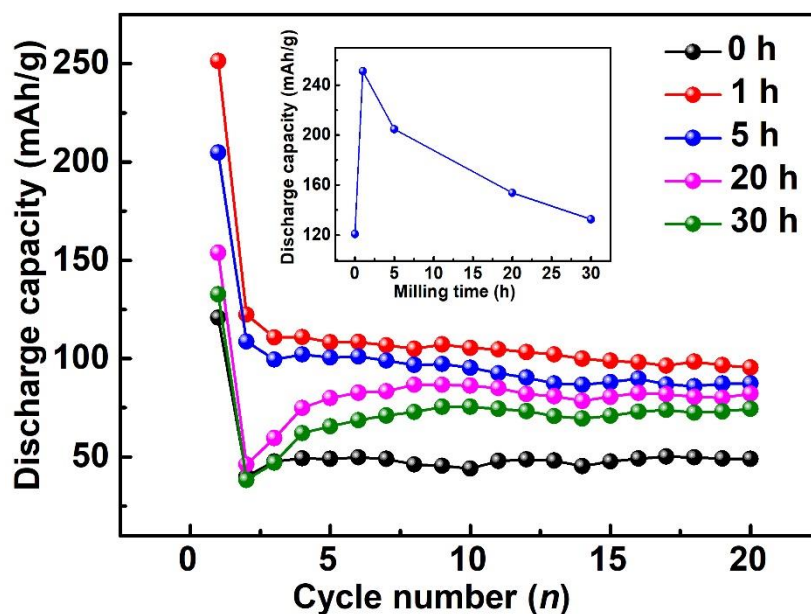


Figure 4. Evolution of discharge capacity of as-milled $Ti_{1.04}Zr_{0.1}La_{0.06}Fe_{0.6}Ni_{0.3}Mn_{0.2}$ alloy.

The 20-cycle charge/discharge current density of 40 mA/g is shown in Fig. 4 for the ball-milled $Ti_{1.04}Zr_{0.1}La_{0.06}Fe_{0.6}Ni_{0.3}Mn_{0.2}$ alloy electrode. After the first cycle, the ball-milled alloy reaches the maximum discharge specific capacity of the cast alloy. The ball-milled alloy has higher activation capacity and discharge specificity. This indicates that ball milling improves the activation and

electrochemical properties of the alloy. The improvement of activation performance is mainly related to the reduction of grain size. HEBM leads to the gradual change of irregular, lumpy particles into spherical particles. The particles decrease in size during the continuous collision, generating many new surfaces, and the increase of specific surface area increases the contact area between the experimental alloy and electrolyte, making the absorption and inward diffusion of hydrogen easier, which helps facilitate the electrochemical reaction process.

Table 1 shows the maximum discharge capacity of the alloy electrodes as cast and with different ball milling time. It can be seen from Table 1 that the discharge capacities of the sample alloys with different ball milling time from 0 h to 30 h are 120.8, 251.3, 204.8, 153.8, and 132.6 mAh/g, respectively. The maximum discharge capacity of as-cast alloy and alloy electrodes first increases and then decreases with ball milling time extension, and the discharge capacity of the alloy after ball milling for 1 h is the largest. The maximum electrochemical discharge capacity of the ball-milled Pr-substituted Ti alloy reported by Zhai et al. [52] was only 170.7 mAh/g, however, the electrochemical capacity after activation of ball-milled La substituted alloy in our paper is significantly higher than that of ball-milled Pr substituted alloy. In addition, the maximum electrochemical capacity of TiFe alloy for 30 h of ball milling reported by Jankowska et al. [45] is only 64 mAh/g. It can be seen that ball-milled La-substituted Ti alloys have a higher electrochemical discharge capacity compared to Pr-substituted Ti alloys. Table 1 gives the maximum discharge capacity of TiFe based alloys modified by different treatment processes. In the literature [19], an attempt was made to improve the discharge capacity of the alloy by elemental Co and Ni substitution, however, it did not achieve the expected results. It was reported in the literature [53] that the maximum discharge capacity of TiFe composite alloys gradually increased with increasing Ni content under the same ball milling time of 80 h, with a maximum discharge capacity of 110 mAh/g. Shang et al. [18] reported that the TiFe alloys prepared by adding Ni composite ball milling showed excellent maximum discharge capacity, with a maximum discharge capacity of 264.2 mAh/g. The prepared TiFe alloy reported in the article [52] was treated with mechanical ball milling and the maximum discharge capacity was not substantially increased, which may be mainly due to the fact that Ni was not added for compounding. In summary, it is clear from the comparison that the addition of Ni or other catalytic elements for compounding by ball milling can significantly increase the electrochemical discharge capacity of the alloy. Therefore, the alloy prepared in our paper was only treated with ball milling process and the maximum discharge capacity of the alloy was 251.3 mAh/g at 1h of ball milling, which has already reached a large discharge capacity. In the next experimental work, the alloy should be mechanically compounded by adding catalyst in order to improve the electrochemical properties of the TiFe alloy to a greater extent. The maximum discharge capacity is related to the surface morphology and structure of the alloy. The high-energy ball milling makes the alloy particles gradually smaller and tends to be spherical, which is conducive to the adsorption and desorption of hydrogen, thereby improving the activation performance of the alloy and the hydrogen absorption capacity of the alloy. However, with the extension of the ball milling time to 5 h, some of the fine spherical particles will be engulfed each other or agglomerate, leading to the average size of the particles being larger again. It makes the inward diffusion of hydrogen difficult and thus the hydrogen storage capacity will be reduced to a certain extent. And when the ball milling reaches 20 h, the phenomenon of particle agglomeration becomes more apparent, the adsorption and diffusion of hydrogen become more

complicated, and the hydrogen storage capacity further decreases. In addition, it is also believed that the decrease in discharge capacity with increasing grinding time is likely to be related to the formation of the amorphous phase. Zeaiter et al. [21] found it to be unfavorably affected by the reversibility of the binding energy between hydrogen atoms and metals. Therefore, the significant decrease in the experimental discharge capacity of the 20 h and 30 h ball-milled alloys is due to an amorphous phase structure. Thus, it can be seen that the activation properties of the alloy can be improved not only by high-energy ball milling but also by a substantial increase in the hydrogen storage capacity. But the longer ball milling time leads to a decrease in the hydrogen storage capacity.

Table 1. Maximum electrochemical discharge capacity (Max-C) of TiFe alloys modified by different treatment processes

Alloys	Max-C (mAh/g)	Reference
Ti _{1.04} Zr _{0.1} La _{0.06} Fe _{0.6} Ni _{0.3} Mn _{0.2} (QM: 0 h)	120.8	Experimental data of this paper
Ti _{1.04} Zr _{0.1} La _{0.06} Fe _{0.6} Ni _{0.3} Mn _{0.2} (QM: 1 h)	251.3	
Ti _{1.04} Zr _{0.1} La _{0.06} Fe _{0.6} Ni _{0.3} Mn _{0.2} (QM: 5 h)	204.8	
Ti _{1.04} Zr _{0.1} La _{0.06} Fe _{0.6} Ni _{0.3} Mn _{0.2} (QM: 20 h)	153.8	
Ti _{1.04} Zr _{0.1} La _{0.06} Fe _{0.6} Ni _{0.3} Mn _{0.2} (QM: 30 h)	132.6	
Ti _{1.04} Fe _{0.7} Zr _{0.1} Ni _{0.1} Mn _{0.1} Pr _{0.06} +10wt.%Ni (QM: 5 h)	264.2	[55]
Ti _{1.04} Fe _{0.7} Zr _{0.1} Ni _{0.1} Mn _{0.1} Pr _{0.06} +10wt.%Ni (QM: 10 h)	247.5	
Ti _{1.04} Fe _{0.7} Zr _{0.1} Ni _{0.1} Mn _{0.1} Pr _{0.06} +10wt.%Ni (QM: 15 h)	230.4	
Ti _{1.04} Fe _{0.7} Zr _{0.1} Ni _{0.1} Mn _{0.1} Pr _{0.06} +10wt.%Ni (QM: 20 h)	221.8	
Ti _{1.04} Fe _{0.7} Zr _{0.1} Ni _{0.1} Mn _{0.1} Pr _{0.06} +10wt.%Ni (QM: 30 h)	133.6	
Ti _{1.04} Pr _{0.06} Fe _{0.6} Ni _{0.3} Zr _{0.1} Mn _{0.2} (QM: 0 h)	52.8	[52]
Ti _{1.04} Pr _{0.06} Fe _{0.6} Ni _{0.3} Zr _{0.1} Mn _{0.2} (QM: 5 h)	170.7	
Ti _{1.04} Pr _{0.06} Fe _{0.6} Ni _{0.3} Zr _{0.1} Mn _{0.2} (QM: 10 h)	134.4	
Ti _{1.04} Pr _{0.06} Fe _{0.6} Ni _{0.3} Zr _{0.1} Mn _{0.2} (QM: 15 h)	127.9	
TiFe (QM: 30 h)	237	[53]
TiFe _{0.9} Co _{0.1} (QM: 30 h)	128	
TiFe _{0.7} Co _{0.3} (QM: 30 h)	108	
TiFe _{0.7} Ni _{0.2} Co _{0.1} (QM: 30 h)	100	
TiMn _{0.9} Fe _{0.55} +0wt.%Ni (QM: 80 h)	4	[54]
TiMn _{0.9} Fe _{0.55} +10wt.%Ni (QM: 80 h)	50	
TiMn _{0.9} Fe _{0.55} +20wt.%Ni (QM: 80 h)	80	
TiMn _{0.9} Fe _{0.55} +30wt.%Ni (QM: 80 h)	110	

Fig. 5 shows the characteristic discharge curves of Ti_{1.04}Zr_{0.1}La_{0.06}Fe_{0.6}Ni_{0.3}Mn_{0.2} alloys with different ball milling times at their respective maximum discharge specific capacities. The discharge characteristic curve is an important performance indicator to characterize the electrode of the hydrogen storage alloy, and the plateau of the discharge voltage in the discharge characteristic curve can evaluate the discharge performance of the alloy. The width of the discharge voltage plateau determines the

discharge capacity of the alloy electrode. The flatness of the discharge plateau is influenced by the homogeneity of the alloy and the catalytic activity of its surface. In general, the discharge characteristic curve of an alloy electrode consists of two segments, one for the extended discharge plateau region, which is the discharge process controlled by the charge transfer rate, and the other for the steep region, which is the region of rapid voltage drop due to the gradual depletion of hydrogen atoms on the surface of the alloy electrode during the discharge process.

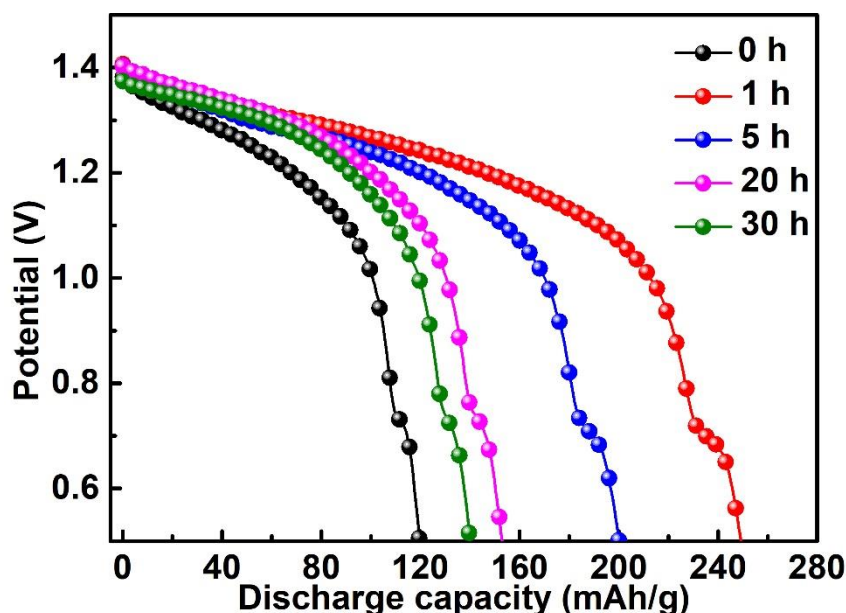


Figure 5. Discharge potential curves of as-milled $\text{Ti}_{1.04}\text{Zr}_{0.1}\text{La}_{0.06}\text{Fe}_{0.6}\text{Ni}_{0.3}\text{Mn}_{0.2}$ alloy.

For the battery, the performance of the discharge voltage will directly affect the output power of the alloy electrode; in other words, if the discharge voltage varies less with capacity, the output power is more stable. It is generally believed that the voltage characteristics are related to the cell's internal resistance determined by the diffusion of hydrogen atoms in the hydride. It can be seen from Fig. 5 that the potential plateau of the discharge characteristic curve of the alloy without ball milling is steep, and the plateau slope is the largest, indicating that the discharge performance is poor. The potential platform area of the alloy after ball milling is flatter than that before ball milling. The platform inclination is smaller, the width of the platform area is more expansive, and the discharge time lasts longer, indicating that the alloy has good discharge performance after ball milling. Among them, the discharge potential platform of the discharge characteristic curve of the alloy electrode after ball milling for 1 h is flat, the width is the largest, and the slope of the platform is the smallest. The plateau trend of ball milling time is getting steeper. It can be seen that too long grinding time is not an effective method to improve performance. Therefore, short-time HEBM is an effective measure to improve the electrochemical performance of hydrogen storage alloys.

3.3 Cycle stability

The capacity retention rate (S_n) can be calculated $S_n = C_n / C_{\max} \times 100\%$ and is an important index used to evaluate the cycle stability of the battery. C_{\max} represents the maximum discharge capacity, and C_n represents the n th discharge capacity. Fig. 6 shows the cycle life curve of the $\text{Ti}_{1.04}\text{Zr}_{0.1}\text{La}_{0.06}\text{Fe}_{0.6}\text{Ni}_{0.3}\text{Mn}_{0.2}$ alloy with different ball milling times with the number of cycles, reflecting the decay process of the discharge capacity. There are several reasons to explain this phenomenon. On the one hand, there is a gradual loss of active material as the reaction proceeds. It is inevitable that the volume of the hydrogen storage alloy will change during charging and discharging. This will cause cracking and chalking on the alloy surface, as well as the formation of harder oxidation and passivation layers. On the other hand, lattice strain and defect formation are the leading causes of stability impairment, while intergranular corrosion is unavoidable [54,55]. Showing that cycle stability is affected by the time spent ball milling, the value of S_{20} can be used as a valuable reference, with a decreasing trend first and then an increase with increasing ball-milling time. More precisely, the sample ball milled for 30 h has S_{20} of 76.4%, which has the highest stability due to an amorphous phase. As reported in the paper by Shang et al. [18], the capacity retention S_{20} of TiFe based alloy ball milled for 30 h with the addition of 10 wt% Ni was 75% after 20 charge/discharge cycles, therefore, the La substituted ball milled TiFe based alloy prepared has superior cycling stability in our paper. In addition, Abrashev et al. [19] concluded that the amorphous phase can significantly enhance the corrosion of the electrode in an alkaline solution, which can effectively inhibit the cracking and efflorescence of the alloy. The nanocrystalline or amorphous alloys have good electrochemical stability and discharge capacity after 30 h of ball milling, reaching 100 mAh/g even after 100 cycles.

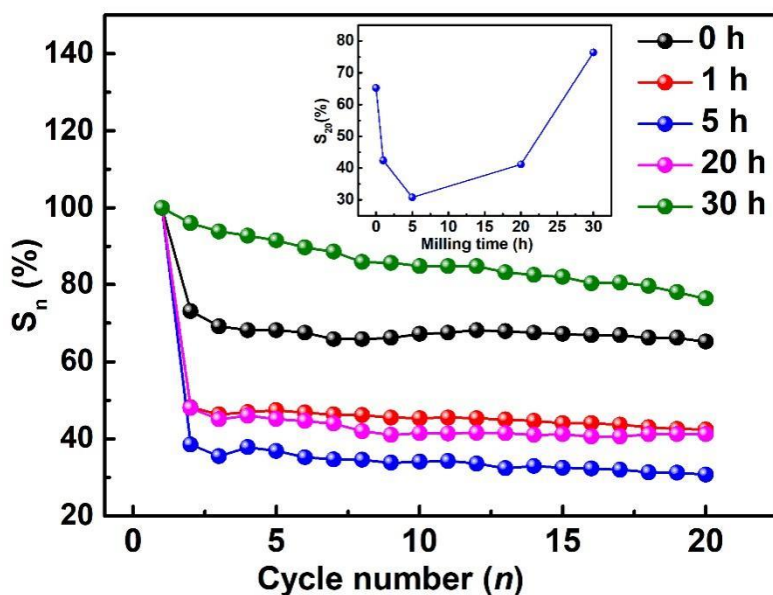


Figure 6. Cycle life curve of as-milled $\text{Ti}_{1.04}\text{Zr}_{0.1}\text{La}_{0.06}\text{Fe}_{0.6}\text{Ni}_{0.3}\text{Mn}_{0.2}$ alloy.

3.4 Kinetics

High rate discharge performance is commonly used to evaluate electrochemical kinetic performance and is measured at different discharge current densities (40, 80, 120, 160, and 200 mA/g). The following equation can calculate the HRD value.

$$HRD = \frac{C_i}{C_{40}} \times 100\% \quad (1)$$

The formula is the discharge capacity when the discharge current density is 40 mA/g. The high-rate discharge curves of the ball-milled $\text{Ti}_{1.04}\text{Zr}_{0.1}\text{La}_{0.06}\text{Fe}_{0.6}\text{Ni}_{0.3}\text{Mn}_{0.2}$ alloy are shown in Fig. 7. The HRD value decreases with the increase of the current density. To illustrate the influence of the ball-milling time on the HRD value, the specific relationship can be seen from the small graph in Fig. 7. The HRD values of the cast and ball-milled alloys first increased from 30.09% to 54.63% and then decreased to 25.94% from 0 h to 30 h. According to the high magnification discharge performance tests of TiFe based alloys reported by Xu et al [56], the HRD values of the alloy electrodes were all very low and the high rate discharge performance was not improved by Pr element substitution. There are two factors that affect the HRD value, including the internal hydrogen diffusivity and charged surface transfer rate. It is necessary to study the effect of ball milling time on hydrogen diffusion and transfer rates. Electrochemical impedance, limiting current density, and hydrogen diffusion coefficient tests were performed below to explore further the reasons that affect the kinetics.

The hydrogen can obtain diffusion coefficient D by measuring the semi-log curve of the current response with time using the constant potential step method. The semi-log curve of current versus time (whole charge state of the alloy) is given in Fig. 7.

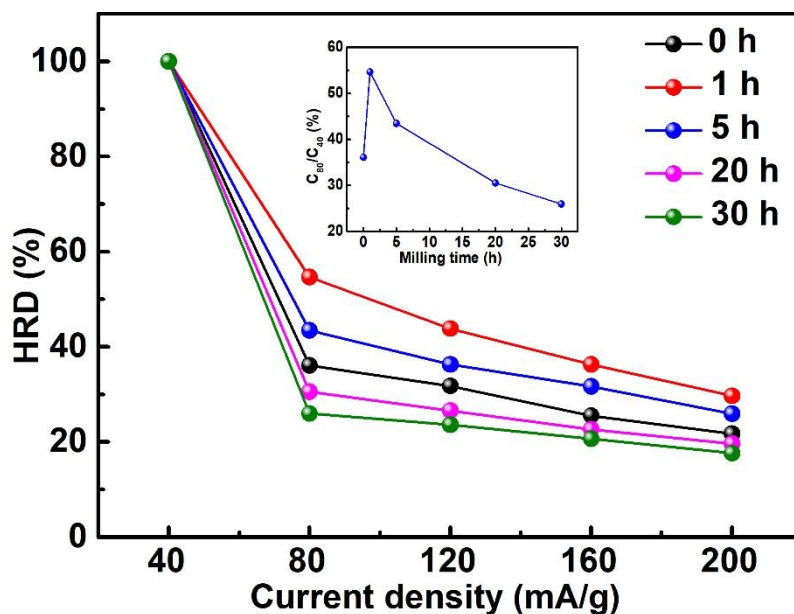


Figure 7. High-rate discharge curves of as-milled $\text{Ti}_{1.04}\text{Zr}_{0.1}\text{La}_{0.06}\text{Fe}_{0.6}\text{Ni}_{0.3}\text{Mn}_{0.2}$ alloy electrode.

It is clear that the initial phase (before 1000 s) $\log i$ decrease significantly, indicating a continuous decrease in the adsorption concentration of hydrogen on the electrode surface due to the oxidation of the electrode. Then the appearance of the linear region in the curve indicates the transfer of the rate control part from the oxidation layer of the electrode to the internal hydrogen diffusion. The hydrogen diffusion can obtain coefficient D by fitting the equation (2), (3) below to the calculated slope of the linear part [18,57].

$$\log i = \log\left(\pm \frac{6FD}{da^2}(C_0 - C_s)\right) - \frac{\pi^2 D}{2.303a^2} t \tag{2}$$

$$D = -\frac{2.303a^2}{\pi^2} \frac{d\log i}{dt} \tag{3}$$

In the formula, D is the hydrogen diffusion coefficient (cm^2/s); i is the diffusion current density (A/g), F is the Faraday constant, C_0 is the initial hydrogen concentration in the alloy (mol/cm^3), and C_s is the surface hydrogen concentration of the alloy particles (mol/cm^3), d is the density of the alloy, a is the radius of the alloy particle (cm), t is the discharge time (s), $\log i$ has a linear relationship with time, which can calculate the D/a^2 value from the slope of the curve, and the hydrogen diffusion coefficient (D) can be obtained by measuring the radius of the alloy particle and bringing it in.

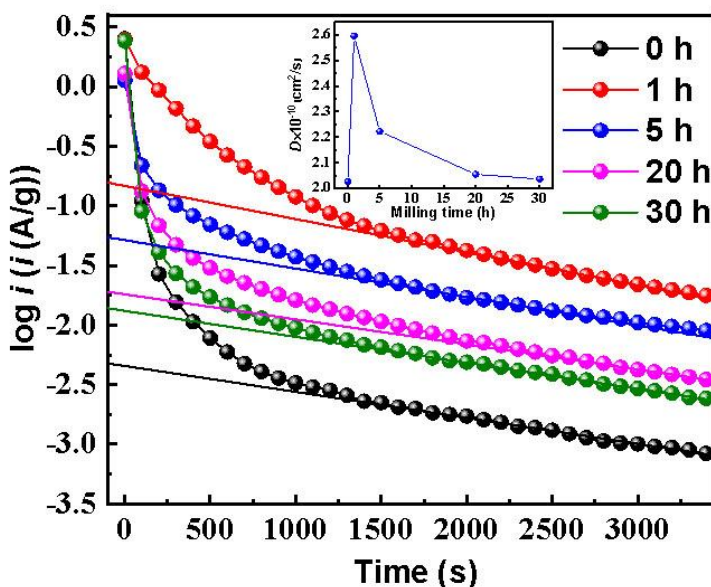


Figure 8. Semi-logarithmic curves of anodic current vs. time responses of as-milled $\text{Ti}_{1.04}\text{Zr}_{0.1}\text{La}_{0.06}\text{Fe}_{0.6}\text{Ni}_{0.3}\text{Mn}_{0.2}$ alloy electrode.

The semi-logarithmic curve of the anodic current versus the time of the ball-milled $\text{Ti}_{1.04}\text{Zr}_{0.1}\text{La}_{0.06}\text{Fe}_{0.6}\text{Ni}_{0.3}\text{Mn}_{0.2}$ alloy electrode is shown in Fig. 8, and the small graph in Fig. 8 indicates the measured D value. It is observed that as the ball milling time increases, the hydrogen diffusion coefficient first reaches its maximum and then decreases, and the D value of the ball-milled alloy was greater than that of the non-ball-milled alloy. Specifically, as the ball milling time increases from 1 h to 30 h, the D value of the ball milled alloy decreases from $2.596 \times 10^{-10} \text{ cm}^2/\text{s}$ to $2.036 \times 10^{-10} \text{ cm}^2/\text{s}$, the decrease in diffusion coefficient was caused by structural alterations, especially the appearance of

amorphous phases and crystal defects. The ability of hydrogen atoms to enter the region is the main reason for several phenomena, including the decrease in crystal defect energy and the increase in the ability of hydrogen atoms to migrate. In addition, the D value at $t = 1$ h is a maximum of 2.596×10^{-10} cm²/s, indicating that ball milling can effectively increase the D value and hydrogen possesses good diffusion ability in the ball-milled alloy at one hour. Moreover, the trend of D value variation coincides perfectly with the trend of high magnification performance, which explains well the high-magnification performance of the electrode.

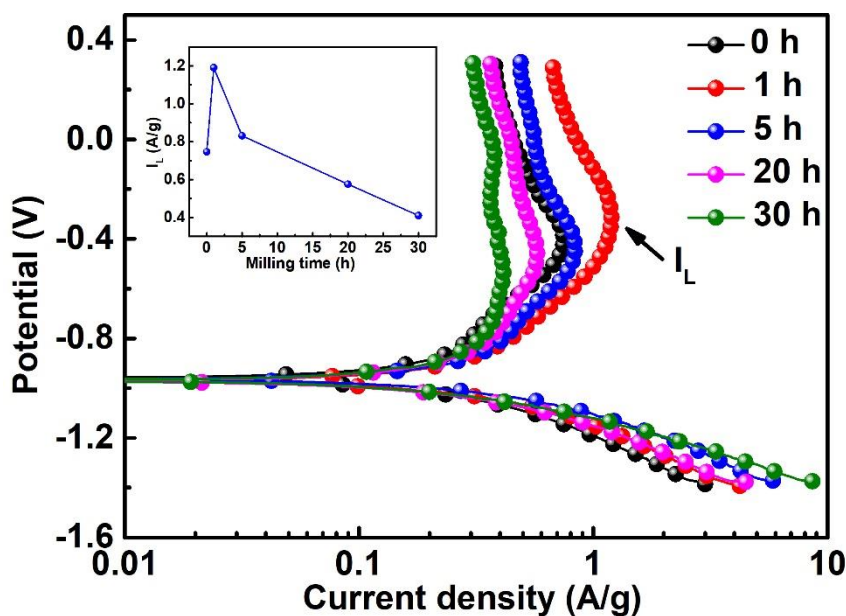


Figure 9. Potentiodynamic polarization curves of as-milled $\text{Ti}_{1.04}\text{Zr}_{0.1}\text{La}_{0.06}\text{Fe}_{0.6}\text{Ni}_{0.3}\text{Mn}_{0.2}$ alloy electrode.

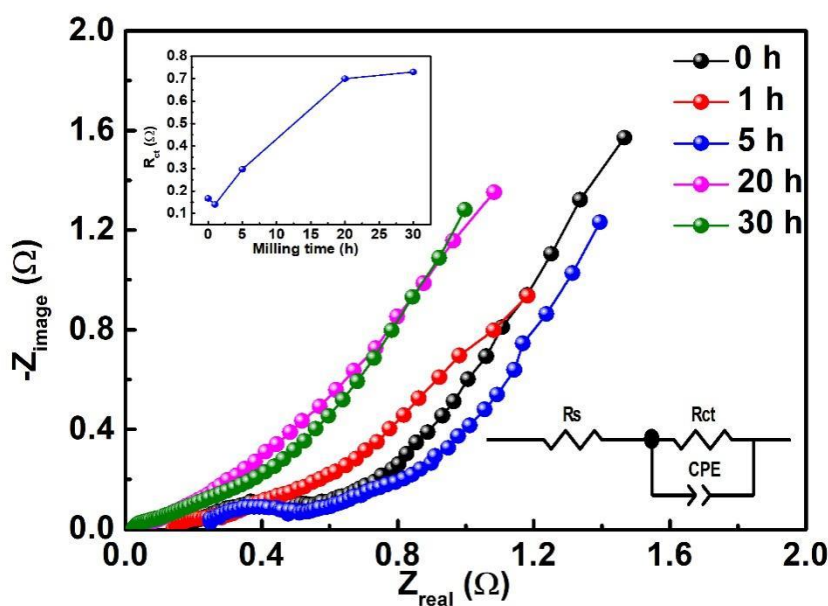


Figure 10. Electrochemical impedance spectra (EIS) of the as-milled $\text{Ti}_{1.04}\text{Zr}_{0.1}\text{La}_{0.06}\text{Fe}_{0.6}\text{Ni}_{0.3}\text{Mn}_{0.2}$ alloy electrode.

Fig. 9 shows the potentiodynamic polarization curve of the ball-milled $\text{Ti}_{1.04}\text{Zr}_{0.1}\text{La}_{0.06}\text{Fe}_{0.6}\text{Ni}_{0.3}\text{Mn}_{0.2}$ alloy electrode. The limiting current density (I_L) is where the polarization curve inverts according to the current density, which reflects the fact that the oxidation reaction on the electrode surface begins to form an oxide layer that hinders the penetration of H atoms into the interior of the experimental alloy [55], therefore, I_L is often considered as the critical current density for passivation. The relationship between the limiting current density and the ball milling time is shown in the small graph in Fig. 9. It can be seen that the I_L value increases at first and then decreases with the increase of the ball-milling time. It is reduced to 0.41 A/g after ball milling for 30 h. In addition, the maximum I_L value is 1.19 A/g when the ball milling time is $t = 1$ h, which indicates that the ball milling has an excellent effect. The trend of the alloy I_L remained basically consistent with its high magnification performance.

The surface charge transfer rate can be characterized by testing the EIS curve of the alloy and the surface charge transfer rate resistance (R_{ct}) obtained by fitting it utilizing the Kuriyama model [48]. Fig. 10 shows the EIS curves of the ball-milled $\text{Ti}_{1.04}\text{Zr}_{0.1}\text{La}_{0.06}\text{Fe}_{0.6}\text{Ni}_{0.3}\text{Mn}_{0.2}$ alloy electrodes, where each curve contains two semicircular arcs and a linear region, with the semicircular arcs in the high and medium frequency regions representing the contact resistance and the surface charge transfer rate resistance (R_{ct}), respectively. In contrast, the straight line in the low-frequency region represents the Warburg impedance. The R_{ct} values can be obtained by fitting with Z-View 2 software. The relationship between its value and the ball milling time is explicitly shown in the small graph in Fig. 10. Ball milling time increased from 0 to 30 h, following which the surface charge transfer rate resistance (R_{ct}) lessened and then increased, decreasing from 0.17 % to 0.14 % and then increasing to 0.7 %. The adverse effect of the increase in surface transfer rate resistance due to the long ball milling time is related to particle refinement. The particle refinement inhibits alloy pulverization during charging and discharging, resulting in a lower transfer rate due to the difficulty of exposing the new electrode surface.

In summary, it can be seen that in the kinetic test, the D and I_L of the experimental alloy with ball milling 1 h have a high level, which is dominant. Although the alternating-current impedance is a secondary factor, it also reflects the high-rate performance of the sample, resulting in the most outstanding *HRD* performance of the ball-milled alloy for 1 h, which has specific guiding significance for the development of battery anode materials with high capacity, rapid dis/charge rate, and the realization of practical industrial application of new energy power.

4. CONCLUSIONS

After a series of studies on the microstructure and electrochemical hydrogen storage performances of the $\text{Ti}_{1.04}\text{Zr}_{0.1}\text{La}_{0.06}\text{Fe}_{0.6}\text{Ni}_{0.3}\text{Mn}_{0.2}$ experimental alloy synthesized by ball milling, the following main conclusions have been drawn:

(1) The as-cast $\text{Ti}_{1.04}\text{Zr}_{0.1}\text{La}_{0.06}\text{Fe}_{0.6}\text{Ni}_{0.3}\text{Mn}_{0.2}$ alloy is composed of the TiFe phase, ZrMn_2 phase, and a small amount of La phase, this crystal structure has a typical shape. However, the diffraction peak gradually broadens, and intensity decreases with the extension of milling time; the ZrMn_2 phase and La phase gradually disappear. The crystalline shape gradually changes to a nanocrystalline or amorphous

structure. The microstructure shows that ball milling can reduce the grain size and refine the grain. In addition, excessively long ball milling can lead to agglomeration.

(2) The activation performance of the ball-milled $\text{Ti}_{1.04}\text{Zr}_{0.1}\text{La}_{0.06}\text{Fe}_{0.6}\text{Ni}_{0.3}\text{Mn}_{0.2}$ alloy is better than that of the as-cast alloy. The discharge capacity of the alloys first increases and then decreases with the milling time increases from 0 to 30 h. The discharge voltage plateau trend of the alloy samples after milling for 1h is flatter, and the first discharge capacity is the highest, which can reach 251.3 mAh/g. In addition, the cycle stability of the sample is the best after 30h ball milling, which is related to the formation of the amorphous phase.

(3) The *HRD* value of ball-milled alloy first increases and then decrease with the extension of ball milling time. The sample ball-milled 1h has the best high-rate discharge performance of 54.63%. The milling time from 0 h to 30 h, the trends of the kinetic parameters (D , I_L and R_{ct}) first increase and then decrease, which is consistent with the variation of *HRD* performance, indicating that short-term HEBM is an effective measure to improve the electrochemical properties of hydrogen storage alloys.

ACKNOWLEDGMENTS

Thanks for the financial of National Natural Science Foundation of China (Nos. 51871125 and 51901105), Natural Science Foundation of Inner Mongolia, China (Nos. 2019BS05005, 2020MS05073, 2021MS05064, and 2022LHMS05018), and Inner Mongolia University of Science and Technology Innovation Fund (2019QDL-B11).

CONFLICT OF INTERESTS

The authors have no relevant financial or non-financial interests to disclose.

References

1. I.P. Jain, *International Journal of Hydrogen Energy*, 34 (2009) 7368.
2. M. Lototsky, I. Tolj, Y. Klochko, M.W. Davids, D. Swanepoel, V. Linkov, *International Journal of Hydrogen Energy*, 45 (2020) 7958.
3. B.P. Tarasov, P.V. Fursikov, A.A. Volodin, M.S. Bocharnikov, Y.Y. Shimkus, A.M. Kashin, V.A. Yartys, S. Chidziva, S. Pasupathi, M.V. Lototsky, *International Journal of Hydrogen Energy*, 46 (2021) 13647.
4. M. Chen, C. Tan, W.B. Jiang, J.L. Huang, D. Min, C.H. Liao, H. Wang, J.W. Liu, L.Z. Ouyang, M. Zhu, *Journal of Alloys and Compounds*, 867 (2021) 159111.
5. C.B. Wan, R.V. Denys, V.A. Yartys, *Journal of Alloys and Compounds*, 889 (2021) 161655.
6. F. Liang, N. Ding, W.Q. Liu, H.Z. Yan, L.M. Wang, *Materials Letters*, 297 (2021) 129945.
7. L. Wang, X. Zhang, S.J. Zhou, J. Xu, H.Z. Yan, Q. Luo, Q. Li, *International Journal of Hydrogen Energy*, 45 (2020) 16677.
8. J.J. Reilly, R.H.J. Wiswall, *Journal of the American Chemical Society, Division of Fuel Chemistry, Preprints*, 53 (1973) 11973.
9. N. Comisso, G. Davolio, E. Soragni, G. Mengoli, *Journal of Electroanalytical Chemistry*, 512 (2001) 92.
10. A.K. Patel, A. Duguay, B. Tougas, C. Schade, P. Sharma, J. Huot, *International Journal of Hydrogen Energy*, 45 (2020) 787.
11. Z.G. Han, Z.M. Yuan, T.T. Zhai, D.C. Feng, H. Sun, Y.H. Zhang, *International Journal of Hydrogen Energy*, 2022, In press. <https://doi.org/10.1016/j.ijhydene.2022.09.227>

12. K. Edalati, J. Matsuda, A. Yanagida, E. Akiba, Z. Horita, *International Journal of Hydrogen Energy*, 39 (2014) 15589.
13. E. Jankowska, M. Jurczyk, *Journal of Alloys and Compounds*, 372 (2004) L9.
14. B. Abrashev, T. Spassov, S. Bliznakov, A. Popov, *International Journal of Hydrogen Energy*, 35 (2010) 6332.
15. V. Zadorozhnyy, S. Klyamkin, M. Zadorozhnyy, O. Bermesheva, S. Kaloshkin, *International Journal of Hydrogen Energy*, 37 (2012) 17131.
16. V.Yu. Zadorozhnyy, S.N. Klyamkin, M.Yu. Zadorozhnyy, O.V. Bermesheva, S.D. Kaloshkin, *Journal of Alloys and Compounds*, 586 (2014) S56.
17. V.Y. Zadorozhnyy, G.S. Milovzorov, S.N. Klyamkin, M.Y. Zadorozhnyy, D.V. Strugova, M.V. Gorshenkov, S.D. Kaloshkin, *Progress in Natural Science*, 27 (2017) 149.
18. H.W. Shang, Y.H. Zhang, J.L. Gao, W. Zhang, X. Wei, Z.M. Yuan, Y.Q. Li, *International Journal of Hydrogen Energy*, 47 (2022) 1036.
19. B. Abrashev, T. Spassov, S. Bliznakov, A. Popov, *International Journal of Hydrogen Energy*, 35 (2010) 6332.
20. H. Emami, K. Edalati, J. Matsuda, E. Akiba, Z. Horita, *Acta Materialia*, 88 (2015) 190.
21. A. Zeaiter, D. Chapelle, F. Cuevas, A. Maynadier, M. Latroche, *Powder Technology*, 339 (2018) 903.
22. H.W. Shang, Y.H. Zhang, Y.Q. Li, Y. Qi, S.H. Guo, D.L. Zhao, *Renewable Energy*, 135 (2019) 14818.
23. P. Lv, *J. Huot. Energy*, 138 (2017) 375.
24. T. Yang, P. Wang, C.Q. Xia, N. Liu, C.Y. Liang, F.X. Yin, Q. Li, *International Journal of Hydrogen Energy*, 45 (2020) 12071.
25. X.H. Wang, R.G. Chen, C.P. Chen, Q.D. Wang, *Journal of Alloys and Compounds*, 425 (2006) 291.
26. H.W. Shang, Y.H. Zhang, Y.Q. Li, J.L. Gao, W. Zhang, X. Wei, Z.M. Yuan, L. Ju, *Journal of Alloys and Compounds*, 890 (2022) 161785.
27. H.W. Shang, Y.Q. Li, Y.H. Zhang, Y.Qi, S.H. Guo, D.L. Zhao, *International Journal of Hydrogen Energy*, 43 (2018) 19091.
28. Y.H. Zhang, H.W. Shang, J.L. Gao, W. Zhang, X. Wei, Z.M. Yuan, *International Journal of Hydrogen Energy*, 46 (2021) 24517.
29. N. Endo, S. Suzuki, K. Goshome, T. Maeda, *International Journal of Hydrogen Energy*, 42 (2017) 5246.
30. H.W. Shang, Y.H. Zhang, Y.Q. Li, Y. Qi, S.H. Guo, D.L. Zhao, *Renewable Energy*, 135 (2019) 1481.
31. B. Hosni, C. Khaldi, O. ElKedim, N. Fenineche, J. Lamloumi, *Journal of Alloys and Compounds*, 781 (2019) 1159.
32. S.M. Lee, T.P. Perng, *Journal of Alloys and Compounds*, 291 (1999) 254.
33. H.W. Shang, Y.Q. Li, Y.H. Zhang, D.L. Zhao, Y. Qi, X.Y. Xu, *International Journal of Hydrogen Energy*, 46 (2021) 17840.
34. Y.Q. Li, H.W. Shang, Y.H. Zhang, P. Li, Y. Qi, D.L. Zhao, *International Journal of Hydrogen Energy*, 44 (2019) 4240.
35. H.W. Shang, Y.H. Zhang, Y.Q. Li, Y. Qi, S.H. Guo, D.L. Zhao, *International Journal of Hydrogen Energy*, 43 (2018) 1691.
36. P. Jain, C. Gosselin, J. Huot, *International Journal of Hydrogen Energy*, 40 (2015) 16921.
37. M. Jurczyk, L. Smardz, K. Smardz, M. Nowak, E. Jankowska, *Journal of Solid State Chemistry*, 171 (2003) 30.
38. H. Miyamura, M. Takada, S. Kikuchi, *Journal of Alloys and Compounds*, 404–406 (2005) 675.
39. A. Seiler, F. Stucki, P. Charpié, *Solid State Communications*, 42 (1982) 337.
40. S.M. Lee, T.P. Perng, *International Journal of Hydrogen Energy*, 19 (1994) 259.
41. Y.Q. Li, H.W. Shang, Y.H. Zhang, P.Li, Y.Qi, D.L. Zhao, *International Journal of Hydrogen Energy*, 44 (2019) 4240.
42. P. Lv, *J. Huot. Energy*, 138 (2017) 375.
43. Z.M. Yuan, T. Yang, W.G. Bu, H.W. Shang, Y. Qi, Y.H. Zhang, *International Journal of Hydrogen*

- Energy*, 41 (2016) 5994.
44. H.Y. Leng, Z.G. Yu, J. Yin, Q. Li, Z. Wu, K.C. Chou, *International Journal of Hydrogen Energy*, 42 (2017) 23731.
 45. E. Jankowska, M Jurczyk, *Journal of Alloys and Compounds*, 346 (2002) L1.
 46. E. Jankowska, M. Makowiecka, M. Jurczyk, *Journal of Alloys and Compounds*, 404–406 (2005) 691.
 47. Y.H. Zhang, Z.G. Han, Z.M. Yuan, T. Yang, Y. Qi, D.L. Zhao, *Journal of Non-Ferrous Metals*, 25 (2015) 3736.
 48. Y.H. Zhang, J.L. Gao, Z.M. Yuan, X. Wei, W. Zhang, Y. Qi, D.L. Zhao, *International Journal of Hydrogen Energy*, 45 (2020) 29023
 49. E. Ulate-Kolitsky, B. Tougas, B. Neumann, C. Schade, J. Huot, *International Journal of Hydrogen Energy*, 46 (2021) 7381.
 50. M. Jurczyk, E. Jankowska, M. Nowak, J. Jakubowicz, *Journal of Alloys and Compounds*, 336 (2002) 265.
 51. M. Jurczyk, E. Jankowska, M. Makowiecka, I. Wieczorek, *Journal of Alloys and Compounds*, 354 (2003) L1
 52. T.T. Zhai, Z.G. Han, Z.M. Yuan, Y.H. Zhang, *Energy Storage Science and Technology*, 10 (2021) 163.
 53. M.J. Choi, H.S. Hong , K.S. Lee, *Journal of Alloys and Compounds*, 358 (2003) 306.
 54. M.V. Simičić, M. Zdujić, R. Dimitrijević, L.J. Nikolić-Bujanović, N.H. Popović, *Journal of Power Sources*, 158 (2006) 730.
 55. G. Zhang, B.N. Popov, R.E. White, *Journal of the Electrochemical Society*, 142 (1995) 2695.
 56. Q.F. Xu, T.T. Zhai, Z.G. Han, Y.H. Zhang. *Metallic Functional Materials*, 28 (2021) 42.
 57. T.T. Zhai, T. Yang, Z.M. Yuan, Y.H. Zhang, *International Journal of Hydrogen Energy*, 39 (2014) 14282.

© 2022 The Authors. Published by ESG (www.electrochemsci.org). This article is an open access article distributed under the terms and conditions of the Creative Commons Attribution license (<http://creativecommons.org/licenses/by/4.0/>).